Enhancement of the photoconversion efficiency of Sb₂S₃ based solar cell by overall optimization of electron transport, light harvesting and hole transport layers

Mohaiyadeen Aliyar Farhana, Jayasundera Bandara [*]

National Institute of Fundamental Studies, Hantana Road, Kandy, Sri Lanka

ABSTRACT

In thin-film photovoltaic, Sb_2S_3 is a leading absorber material due to its broad-band optical response and excellent electrical properties, with the highest reported efficiency in the planar Sb_2S_3 configuration being 8 %. By simulations, optimized parameters for each component of the *n*-i-p FTO/ETL/Sb_2S_3/HTL/Au planar heterojunction device, as well as a photoconversion efficiency (PCE-η) of 28.64 % under an AM 1.5G spectral irradiance, have been predicted. In this report, we systematically optimized the electron transport layer (ETL), light harvesting layer (Sb_2S_3), and hole transport layer (HTL) separately based on theoretically predicted values in order to understand the effect of each component and optimize solar cell performance. The optimized results showed that simply optimizing the ETL, Sb_2S_3 layer, and HTL resulted in achieving the efficiency ~4.11 % and to achieve the theoretically predicted device performance, a precise control of intrinsically formed traps, the presence of surface defect states, and lattice dislocations in Sb_2S_3, are important as these factors are found to be the main factors that enhance charge carrier recombination, slow charge transfer across the interface, and charge carrier mobility.

1. Introduction

Cadmium sulfide (CdS), lead sulfide (PbS), Cadmium Telluride (CdTe), copper indium gallium selenide (CIGS), kesterite (CZTS), and antimony sulfide (Sb_2S_3) semiconductors have all been studied extensively as light-absorbing layers in solid-state solar cell applications. (Brennan et al., 2011; Lu et al., 2018; Tian et al., 2013; Xu et al., 2014; Lakhe et al., 2016; Wang et al., 2019; Shah et al., 2021) Despite, the fact that PCEs of 22.1 and 23.4 % have been achieved in the laboratory scale for CdTe and CIGS, respectively, the scarcity of Ga and In, as well as the toxicity of Cd, Se, and Te, motivate researchers to look into new light-harvesting materials that are less toxic and abundant. (Powalla et al., 2017; Green et al., 2020) In this respect, Sb_2S_3 is advantageous due to the availability and nontoxicity of the constituent elements, low melting point (~550 °C), high absorption coefficient (1.8×10^5 cm^{-1} at 450 nm), suitable bandgap energy (~1.7 eV), good stability in air/moisture, and high charge carrier diffusion lengths. (DeAngelis et al., 2016; Eensalu et al., 2019; Eensalu et al., 2019).

In 1993, Savadogo et al. fabricated the first planar Sb_2S_3 solar cell with a PCE of 5.19 % by depositing a ~2 μm thick Sb_2S_3 film using the CBD method on a (1 1 1) oriented p-type Si substrate and annealing it at 350 °C under N₂ atmosphere. (Savadogo and Mandal, 1994) The Sb_2S_3 planner solar cell with a front-contact/ETL/Sb_2S_3/HTL/back-contact device structure is currently popular due to their simpler structure, and as a result, much research has been focused on it to improve device performance.[13b] Because the morphology of Sb_2S_3 thin film has been discovered to be one of the critical factors that contribute to the device performance, solar cells with thin Sb_2S_3 films with different nanostructures such as smooth and textured have been fabricated using a variety of methods, and a highest PCEs of 7.5, 7.1, 5.5, 3.8, 4.17, and 5.7 % have been reported for chemical bath deposition (CBD) (Choi et al., 2014), spin coating (Han et al., 2019), spray pyrolysis (Eensalu et al., 2019), close space sublimation (Guo et al., 2019), thermal evaporation (Yuan et al., 2017), and atomic layer deposition (ALD) (Kim et al., 2014) of Sb_2S_3 films respectively. However, neither chemical nor physical methods of producing Sb_2S_3 films yielded satisfactory solar cell performance. The highest reported efficiency of ~7 % with V₍oc₎ (open-circuit voltage), J₍sc₎ (short-circuit current), and FF (fill factor) and η (power conversion efficiency). of ~700 mV, ~18 mA/cm² and ~57 %, respectively for FTO/ETL(TiO₂)/Sb_2S_3/SbCl₃/Spiro/Au planar configuration.

Surface defect states in Sb_2S_3, which cause slow charge transfer across interfaces and intrinsically formed traps that enhance charge carrier recombination, have been identified as a barrier to improving device performance. (Courel et al., 2019; Cao et al., 2020; Xiao et al., 2020; Cai et al., 2020) Improved solar cell performance has been reported using interfacial (Choi et al., 2014; Büttner et al., 2021; Xu et al., 2018; Shi et al., 2021) band-gap engineering (Li et al., 2020; Horoz and Sahin, 2017), additive engineering (Zhou et al., 2021), and defect passivation in Sb_2S_3. (Han et al., 2019; Maiti et al., 2019; Dong et al., 2021).

Despite the fact that all of these changes were reported to improve device performance, the highest reported efficiency of 7 % is much inferior to the theoretically predicted PCE of ~28.64 %, (with J_{SC} = 22.46 mA/cm^2, V_{OC} = 1.402 V, FF = 91 %) under an AM 1.5G spectral irradiance for single p-n junction with an absorber of 1.7 eV. (Rühle, 2016) Based on the simulation work, significant roles of ETL, Sb_2S_3 and HTL have been demonstrated, i.e in the full-inorganic FTO/ZnS/Sb_2S_3/HTLs/Au device structure, the optimized parameters of each component have been predicated. (Xiao et al., 2020; Islam and Thakur, 2020) In a different simulation study, it has been reported that the buffer layer depended on the thickness of Sb_2S_3 film, with the optimal thickness of Sb_2S_3 being 1.5–1.8 μm for ZnS while it was found to be 2–4 μm for CdS and TiO$_2$.. (Islam and Thakur, 2020) Similarly, the best PCE of the Sb_2S_3 cell with the CBM$_{ETL}$ and VBM$_{HTL}$ at −3.5 eV and −6.1 eV, respectively, has been suggested by investigating the effect of the relative positions of the CBM$_{ETL}$ vs the work function of the front electrode and VBM$_{HTL}$ vs the work function of the back contact. (Cao et al., 2020) Furthermore, an ETL with a conduction band minimum of −4.4 eV < CBM < -3.2 eV and a HTL with a valence band maximum of –5.2 eV > VBM > − 6.4 eV have been predicted for an efficient carrier transfer process for the Sb_2S_3 absorber layer.

Overall, by the simulation results, the importance of having a proper and lower Sb_2S_3 film thickness (~0.8 − 1.5 μm) than the carrier diffusion length (L_D ~ 1.6 μm) to facilitate the conversion of photo-generated electron-hole pairs to photo-generated current, has been identified. Furthermore, defects in Sb_2S_3 have been identified as a significant limiting factor for device performance. (Courel et al., 2019; Xiao et al., 2020) Similarly, up-to-date simulation results strongly suggest factors that should be considered when selecting the ETL and HTL are the non-ideal band alignment, the formation of Schottky contacts, element diffusion, and the formation of defects at the semiconductor/metal contact. Despite the fact that simulation investigations of various device parameters of Sb_2S_3 solar cells pave the way for improved solar cell performance, to the best of our knowledge, no concerted effort has been made to exploit theoretical predictions of Sb_2S_3 solar cell performance. As a result, in this study, we systematically investigated the solar cell performance of Sb_2S_3 solar cells by optimizing the ETL, light harvesting Sb_2S_3 layer, and HTL thicknesses as the thickness of these layers are highly related to device performance factors such as carrier diffusion length, band alignment, the formation of Schottky contacts, element diffusion, and the formation of defects at the semiconductor/metal contact. As CdS and TiO$_2$ are the most common ETLs and P3HT and SpiroOMeTAD are the most common HTLs (Eensalu et al., 2019; Zeng et al., 2018), we used the FTO/ETL(TiO$_2$)/Sb_2S_3/HTL(P3HT)/Ag device structure in our study for systematic optimization based on simulation predictions.

2. Experimental section

2.1. Preparation of electron transport layer (ETL)

The 0.25 mM of TiO$_2$ precursor was prepared by mixing 75 of titanium(IV) isopropoxide(TTIP, Fluka, 97 %) in a mixture of 50 μl of diethanolamine (C$_4$H$_{11}$NO$_2$, Research Lab, 99 %) and 910 μl of butan-1-ol (C$_4$H$_{10}$O, BDH, 99 %). The prepared solution was spun coated on a cleaned fluorine doped tin oxide (FTO, 7 Ωcm^{-2}, Solaronix)(1 × 2.5 cm) at 3000 rpm for 30 s and the thickness of the TiO$_2$ layer was varied by

using different number of spinning cycles (i.e 1–5 spinning cycles). After each spinning, the coated layers were heated for 5 mins at 180 °C on a hot plate. Finally, the cells with TiO$_2$ layers were heated in the furnace for 1 h at 500 °C in air. Once the optimum TiO$_2$ thickness is decided by selecting the number of spinning cycles, the optimized spinning cycles of TiO$_2$ layer were used for further study on Sb_2S_3 solar cells. All the solutions were prepared in air unless specified.

2.2. Fabrication of Sb_2S_3 layer

The light-harvesting Sb_2S_3 precursor was prepared by dissolving 228 mg (1 mmol) of antimony chloride (SbCl$_3$, MACKLIN, 99 %) and 114 mg (1.5 mmol) of thiourea (TU, ACROS Organics, 99+%) in 1 ml of 2-methoxyethanol (2-ME, ACROS Organics, 99 %). The prepared solution was spin coated on TiO$_2$ layer for 30 s at various spinning speeds (2000–6000 rpm) in air. The coated Sb_2S_3 layers were pre-heated on the hot plate at 150 °C for 1 min just after the spinning, followed by annealing inside the tube furnace at 280 °C for 10 mins with a N$_2$ flowing rate of 5 ml/min. The thickness of the Sb_2S_3 layer was changed by spinning the 20 μl of Sb_2S_3 precursor solution by varying the spinning speed from 2000 to 6000 rpm.

2.2.1. Preparation of hole-transport layer (HTL)

Three hole-transport layers were employed and these hole transport layers were prepared as follows; (a) P3HT- 2 mg of poly(3-hexylthiophene-2,5-diyl (P3HT, Luminescence Technology, 94 %) was dissolved in 100 μl of chlorobenzene (ACROS Organics, 99+%) and 20 μl of prepared hole transport solution was spin coated on FTO/TiO$_2$/Sb_2S_3 for 30 s at 3000 rpm. The coated layers were heated on the hot plate at 100 °C for 20 min in air, (b) SpiroOMeTAD- 3.6 mg of SpiroOMeTAD was dissolved in 100 μl of chlorobenzene, and 0.8 μl of Li$^+$ solution and 1.4 μl of 4-*tert*-Butylpyridine (TBP, Sigma-Aldrich, 98 %) were added. The Li$^+$ solution was prepared by adding 520 mg of Bis(trifluoro-methane)sulfonimide (LiTFSI, Sigma-Aldrich, 99.95 %) in 1 ml of acetonitrile (Sigma-Aldrich, 99 %). The prepared 20 μl of Spiro solution was spin coated on Sb_2S_3 for 30 s at 3000 rpm. The coated cells were heated on hotplate at 100 °C for 20 min in air, (c) CuSCN- 20 mg of CuSCN was dissolved in 1 ml of 2-Ethylsulfide (Sigma-Aldrich, 98 %) and 20 μl of prepared CuSCN solution was spin coated for 30 s at 2500 rpm with two spinning cycles. After every spinning, the cells were heated on the hotplate at 100 °C for 20 min in air.

2.3. Device fabrication

The planar configuration of Sb_2S_3 solar cells (FTO/TiO$_2$/Sb_2S_3/P3HT/Ag) was fabricated for this study. A 70 nm Silver (Ag, Sigma-Aldrich, 99.9 %) layer was deposited as a counter electrode by the thermal evaporation technique under 1 × 10^{-5} Torr.

2.4. Characterization

The absorption spectra of the films were recorded by a UV–vis spectrophotometer (Shimadzu 2450) in a wavelength range of 300 to 800 nm. Cyclic voltammetry (CV) and Mott-Schottky experiments were carried out in a one-compartment three-electrode cell by using the ZahnerZannium universal electrochemical work station equipped with a frequency response analyzer (Thalas) at 10 mV amplitude AC signal and at the frequency 1 KHz in dark. Photocurrent and voltage measurements and electrochemical impedance spectroscopy (EIS) were obtained using Metrohm Autolab under the illumination of 100 mW cm^{-2} with AM 1.5 spectral filter. The IV curves External quantum efficiency (EQE) curves were measured as a function of wavelength from 300 to 800 nm using the Bentham PVE300 photovoltaic measurement setup. For IV and IPCE measurements, five solar cell devises were tested and average values were taken. Morphology measurements of the prepared Sb_2S_3 films were performed using ZEISS EVO scanning electron microscope.
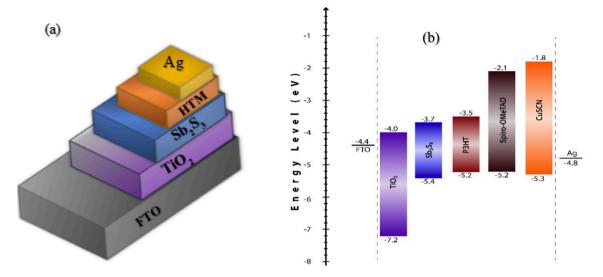
Fig. 1. (a) Device structure of heterojunction solar cells with ETL, Sb$_2$S$_3$ and HTL and (b) The corresponding energy level diagram (under illumination) of the Sb$_2$S$_3$ solar cell device.
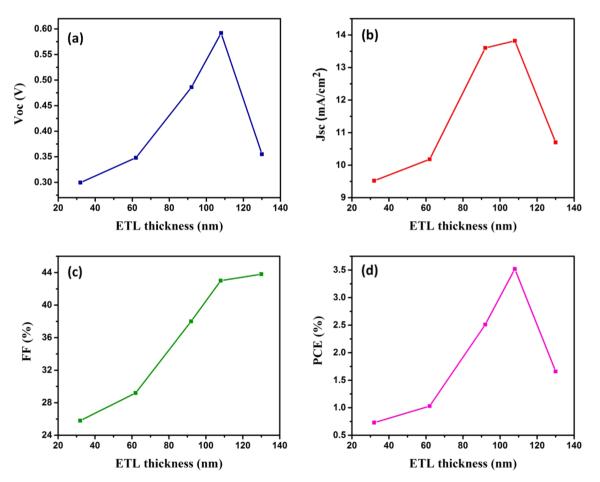

Fig. 2. The variation of (a) Voc, (b) Jsc, (c) FF and (d) η with the variation of the thickness of the TiO$_2$ layer.

3. Results and discussions

We used the FTO/ETL/Sb$_2$S$_3$/HTL/Ag the device structure in our study for systematic optimization based on simulation predictions. Based on theoretical simulations, the best PCE of the Sb$_2$S$_3$ cell has been predicted with the CBM$_{ETL}$ and VBM$_{HTL}$ at −3.5 eV and −6.1 eV respectively, and thus TiO$_2$ and P3HT were chosen as ETL and HTL as

their CBM$_{ETL}$ and VBM$_{HTL}$ are within the theoretically predicted energy positions. The optimized TiO$_2$ (ETL), Sb$_2$S$_3$ (light harvesting layer) and P3HT (HTL) thicknesses of full-inorganic FTO/TiO$_2$/Sb$_2$S$_3$/P3HT/Ag device structure by simulations were 0.05–0.1 μm, ~0.8 μm and ~0.1 μm, respectively. (Xiao et al., 2020; Islam and Thakur, 2020; Zhou et al., 2018; Yaghoobi Nia et al., 2019) The schematic diagram of the designed structure and their energy levels are shown in Fig. 1 (a) and (b).

Table 1

TiO$_2$ thickness-dependent photovoltaic performance of the devices FTO/TiO$_2$/Sb$_2$S$_3$/P3HT/Ag measured under one Sun AM 1.5G illumination. Voc, Jsc, FF and η stand, respectively, for the open-circuit voltage, short-circuit current, fill factor and power conversion efficiency. The layer thickness of Sb$_2$S$_3$ and P3HT kept at ~380 nm and ~80 nm respectively.

Thickness of the TiO$_2$ ETL layer (nm)	J$_{SC}$ (mA/cm^2)	V$_{OC}$ (mV)	FF (%)	η (%)
32	9.52	299.5	25.8	0.73
62	10.18	348.1	29.2	1.03
91	13.60	486.2	38.0	2.51
108	13.82	592.0	43.0	3.52
130	10.7	355.1	43.8	1.66

During the optimization process, we first prepared the cells with varying the TiO$_2$ thicknesses from ~30 to ~130 nm by varying the number of TiO$_2$ spinning cycles (1–5) to optimize the ETL thickness while keeping the Sb$_2$S$_3$ and P3HT layer thicknesses at ~380 nm and ~80 nm respectively for each cell. The TiO$_2$ layer thickness was determined using cross-sectional SEM images of TiO$_2$ deposited on the FTO substrate (Figure S1), and the effect of the ETL layer thickness on the Voc, Jsc, FF, and of the FTO/TiO$_2$/Sb$_2$S$_3$/P3HT/Ag device is illustrated in Fig. 2 and summarized in Table 1. The photovoltaic parameters shown in Fig. 2 show that Voc, Jsc, FF, and efficiency increase with the increase of ETL layer thickness up to ~105 nm, and increasing the ETL layer further results in a decrease in overall solar cell performance, and these results are consistent with the theoretically predicted thickness dependence ETL behavior.

The significant role of the TiO$_2$ ETL for charge carrier transport and recombination was assessed by analyzing the cyclic voltammetry (CV) of different thicknesses of TiO$_2$/FTO working electrode in the aqueous Fe(CN)$_6^{3-/4-}$ electrolyte, where the voltammogram represents the redox (oxidation–reduction) reaction between Fe(CN)$_6^{3-}$ and Fe(CN)$_6^{4-}$ is used as an index to explain the blocking effect of TiO$_2$ layer. As the redox potential of Fe(CN)$_6^{3-/4-}$ is sufficiently positive to the flat band potential of TiO$_2$ (rutile and anatase) in all the practically accessible pH values in aqueous solutions, the peak to peak voltage and current density difference of the CV is the indication of the electron recombination at a given pH value. As shown in Fig. 3a, in the CV of bare FTO, the peak to peak voltage and current density differences are 0.1 V and 0.75 mAcm^{-2} respectively. However, the decrease in peak to peak current density and increase in the voltage difference with the increase of the thickness of TiO$_2$ layer up to ~108 nm is an indication of the enhancement of charge blocking properties of TiO$_2$ resulting in reduced charge recombination

and an improvement in open circuit voltage (Voc) and device performance. However, further increase in TiO$_2$ layer thickness resulting in the rapid decrease in Voc and Jsc while FF remains nearly the same, which could be assigned to the increase in series resistance of a thicker TiO$_2$ layer which is supported by the calculated higher series resistance of the thicker TiO$_2$ layer (215 Ωcm^2) compared to that of thinner TiO$_2$ layer (43 Ωcm^2) for the IV shown in Fig. 3b. Hence, at thicker TiO$_2$ layer, charge trapping may result in increasing the charge recombination and consequently the observed lower solar cell performance can be justified.

In the optimization of ETL, the highest solar cell efficiency of 3.53 % was observed for 105 nm thick ETL together with the with the Sb$_2$S$_3$ (~380 nm) light harvesting material and the P3HT (~100 nm) HTL with V$_{oc}$, J$_{sc}$ and FF of 592 mV, 13.82 mA/cm^2 and 43 % respectively. Having optimized the ETL thickness, as charge carrier generation and dissociation are important processes for photocurrent generation, the properties of the light harvesting Sb$_2$S$_3$ layer were investigated.. In the optimization of Sb$_2$S$_3$ layer thickness on the solar cell performance, the layer thickness of ETL was kept at 105 nm and the HTL thickness at ~100 nm and Sb$_2$S$_3$ layer thickness was varied from 175 to 650 nm. The formation of crystalline stibnite Sb$_2$S$_3$ was confirmed by XRD analysis and as shown in Figure S2, the XRD peaks at 10.0°, 15.7°, 17.6°, 22.4°, 25.0°, 28.6°, 32.1° and 35.6° of Sb$_2$S$_3$ film which was annealed at 280°C can be indexed to orthorhombic stibnite Sb$_2$S$_3$ (JCPDS PCPDFWIN #42–1393) (1 1 0), (020/200), (1 2 0), (2 2 0), (1 3 0), (230/320), (0 2 1) and (240/420) respectively. Fig. 4 depicts the variation of Voc, Jsc, FF, and η of devices fabricated with varying thicknesses of Sb$_2$S$_3$ layers, and Table 2 summarizes the measured performance.

As shown in Fig. 4, the efficiency increases as the thickness of Sb$_2$S$_3$ increases from ~175 to ~270 nm and then decreases as the Sb$_2$S$_3$ thickness increases further. The photovoltaic parameters shown in Fig. 4 indicates that Voc, Jsc, FF, and η increase with increasing Sb$_2$S$_3$ layer thickness up to 270 nm, and at the maximum thickness, a 4.01 % PCE with 619.2 mV of VOC, 14.05 mA/cm^2 of JSC and 46.1 % of FF has been observed. Further increasing the thickness of the Sb$_2$S$_3$ layer reduces the overall solar cell performance, which is consistent with the theoretically predicted thickness dependence Sb$_2$S$_3$ behavior and can be explained as follows. As shown in Fig. 5a, Sb$_2$S$_3$ layers exhibit a significant amount of absortion in the visible region (400–800 nm) and the change in Sb$_2$S$_3$ thickness and morphology (Figure S3) could absorb more photons which could enhance the photocurrent. The estimated energy gap of crystalline Sb$_2$S$_3$ film by the plot of (αhν)^{2}Vs hν (Fig. 5c) was 1.69 eV, which was very close to the literature reported Eg value of Sb$_2$S$_3$. Additionally, the absorption of the FTO/TiO$_2$/Sb$_2$S$_3$/P3HT/Ag device was further improves due to the contribution of P3HT HTL (Fig. 5b).
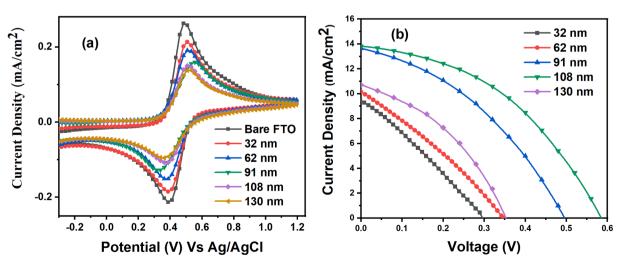

Fig. 3. (a) Cyclic voltammograms for the bare FTO and TiO$_2$ coated on FTO with various TiO$_2$ layer thicknesses; scan rate: 50 mV/s, electrolyte solution: 0.5 mM Fe(CN)$_6^{3-/4-}$ in aqueous 0.5 M KCl, pH 1.5 (b) J-V characteristics of FTO/TiO$_2$/Sb$_2$S$_3$/HTL with TiO$_2$ layer thickness.
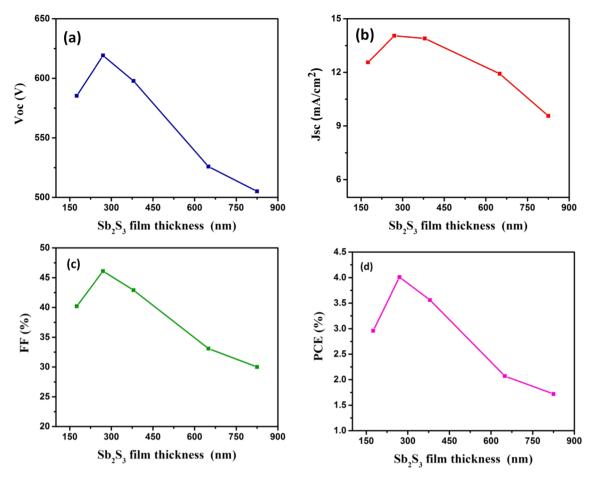
Fig. 4. The variation of (a) Voc, (b) Jsc, (c) FF and (d) η with the variation of the thickness of the Sb_2S_3 layer.

Table 2
Sb_2S_3 layer thickness dependent photovoltaic performance of the devices FTO/TiO_2/Sb_2S_3/P3HT/Ag measured under one Sun AM 1.5G illumination. The layer thickness of ETL and P3HT kept at ~105 nm and ~80 nm respectively.

Thickness of the Sb_2S_3Layer (nm)	J_{SC} (mA/cm^2)	V_{OC} (mV)	FF (%)	η (%)
825	9.56	505.1	33.0	1.59
650	11.92	525.9	33.1	2.07
380	13.9	597.8	42.9	3.56
270	14.05	619.2	46.1	4.01
175	12.56	585.3	40.2	2.96

Fig. 5d and e show the variations of JV and EQE respectively with Sb_2S_3 thickness variation. When the changes in Voc, Jsc, and FF are compared to the variation in Sb_2S_3 film thickness, it can be seen that the device performance is significantly dependent on J_{sc} compared to V_{oc} or FF, which in turn is highly dependent on the light harvesting efficiency and the thickness of Sb_2S_3 film. The light harvesting efficiencies of Sb_2S_3 films can be estimated according to the Beer-Lambert law $I(x) = I_0\ e^{-ax}$, in which the I_0 is the incident photon flux and the $I(x)$ is the photon flux in Sb_2S_3 and taking the absorption coefficient α of Sb_2S_3 as 10^5 cm^{-1} in the visible region. (Wu et al., 2019) Accordingly, with Shockley-Queisser balance limit for a single p-n junction with a compact Sb_2S_3 absorber and a 1.7 eV bandgap, 175, 270, 380, 650, and 825 nm thick Sb_2S_3 layers could absorb 82, 93, 96, 98 and 100 % of incoming light respectively and Jsc is expected to increase linearly with the increase of Sb_2S_3 thickness generating 18.5, 20.9, 21.7, 22.3, and 22.4 mA/cm^2 respectively under an AM 1.5G spectral irradiance. Contrary, when the thickness increases from 175 nm to 270–380 nm, Jsc increases from to

12.5 to 14.5–13.9 mA/cm^2 but when the thickness increases to 650 nm, Jsc decreased to 11.9 mA/cm^2 and when the thickness increases further to 800 nm in which the light absorption efficiency is 100 %, the device Jsc is sharply decreased to 9.5 mA/cm^2 (Fig. 5d). These findings support that Jscs do not increase linearly with increasing the Sb_2S_3 film thicknesses, implying that absorption could not be the only factor influencing the Jsc. According to Wu et al., absorption plays a significant role in thinner Sb_2S_3 films where the thickness is less than the hole transport length and absorption and the internal electric field are the primary factors influencing the photocurrent, whereas transport is the primary cause of photocurrent decrement when the thickness is greater than the hole transport length. (Wu et al., 2019).

As shown in Fig. 5e, the overall EQE response increase with the increase of Sb_2S_3 thickness from 170 nm to 270 nm and further increase in Sb_2S_3 thickness results in decrease in the EQE response. The decrease in EQE response of thicker Sb_2S_3 films i.e. 380–850 nm cannot be understood purely considering the hole diffusion lengths as the hole diffusion length of Sb_2S_3 is 1.6 μm. Hence, the presence of defects and interfacial contacts may significantly reduce the hole-diffusion length and consequently hole collecting efficiency resulting in a reduced EQE response for Sb_2S_3 films thicker than ~300 nm, as illustrated in Fig. 5c. Consequently, the balance between the electron and hole diffusion lengths determines the maximum Sb_2S_3 thickness of 270 nm. Interestingly, the EQE spectra shown in Fig. 5(e), shows that increasing the Sb_2S_3 thickness above 650 nm results in a drastic decrease in response for wavelengths greater than 600 nm, resulting in a decrease in Jsc, whereas the change in Jsc is comparatively less pronounced below 600 nm because more light is already absorbed in the Sb_2S_3. The behavior of thick Sb_2S_3 films in response to short and long wavelengths can be explained using light diffusion lengths. Long waves can diffuse to the far end of a 650 nm
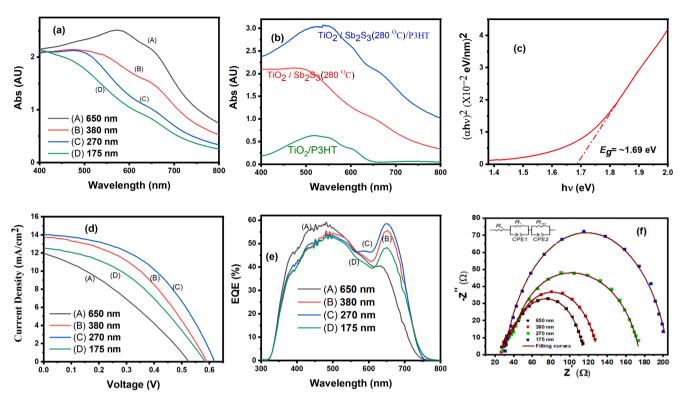
Fig. 5. (a) UV–vis absorption spectra of Sb_2S_3 film with the variation of Sb_2S_3 thickness, (b) UV–vis absorption spectra for the TiO_2//P3HT, TiO_2/Sb_2S_3 and TiO_2/Sb_2S_3/P3HT, (c) Tauc plot of the optical absorption spectra of the crystalline Sb_2S_3, (d) J-V characteristics of FTO/TiO_2/Sb_2S_3/HTL with the variation of Sb_2S_3 layer thickness at AM 1.5 (1000 W/m^2), (e) corresponding IPCE with the variation of Sb_2S_3 layer thickness and (f) EIS plot (inset shows the equivalent circuit) of the devices with the variation of Sb_2S_3 thicknesses.

Table 3
Fitting results of the EIS spectra of the devices with different thickness of Sb_2S_3 layer.

Thickness of Sb_2S_3 layer (nm)	Rs (Ωcm^2)	Rt (Ωcm^2)	R_{Rec} (Ωcm^2)	τ (μs)
650	27.5	9.43	77.9	4.72
380	28.5	8.93	100.4	4.86
270	29.2	7.56	138.8	6.82
175	30.3	5.01	140.8	4.69

Sb_2S_3 thick film because their illumination depths are greater than that of short wavelengths due to their lower absorption coefficient, and thus holes generated in close proximity of the cathode by long wavelength excitation are efficiently collected. (Wu et al., 2019) As a result, the observed EQE response increase in the long wavelength region is justifiable. The observed increase in EQE in the long wave region in this investigation cannot be mainly attributed to the parasite light effect of P3HT as explained in several research groups for thin Sb_2S_3 films. For a 400–600 nm thick Sb_2S_3 film, as P3HT does not receive light due to most photons are absorbed by Sb_2S_3 and it only serves as a hole transport layer to collect holes.

The observed Voc, Jsc, FF and η for the optimized ETL and Sb_2S_3 are significantly lower than the theoretically predicted solar cell performance for a single p-n junction, which may be attributed to recombination mechanisms at both the bulk and interface of the Sb_2S_3, a non-ideal band alignment, or the formation of defects at the semiconductor/metal contact. Impedance spectroscopy measurements were performed to better understand the differences in solar cell performance observed as Sb_2S_3 thickness varied. The Nyquist plots for the FTO/TiO_2/Sb_2S_3/P3HT solar cells measured under one-sun illumination are shown in Fig. 5f, and the EIS data is fitted with a simplified equivalent circuit shown in the inset in Fig. 5f and the fitting results summarized in

Table 3. The simplified equivalent circuit was employed as the FTO/TiO_2/Sb_2S_3/P3HT device structure is similar to a planar heterojunction solar cell and the equivalent circuit consists of series resistance (Rs), a hole transport and extraction resistance (Rt) at selective electrode, a recombination resistance (Rrec), and two constant phase angle elements (CPE). The small arc at high frequency on the Nyquist plots represents hole transport and extraction resistance (Rt) at the cathode, whereas the main arc at low frequency represents recombination resistance (Rrec) in the devices. As given in Table 3, when the Sb_2S_3 film thickness increases, the gradual increase in Rt can be noted. i.e. when the Sb_2S_3 thickness increased from 175 to 650 nm, the Rt increased from 5 to 9.5 Ω cm^2, indicating the ease of transport and extraction of holes at the Ag cathode with thinner Sb_2S_3 films than with thicker Sb_2S_3 films. Furthermore, the higher Rrec value of a 175 nm thin Sb_2S_3 film (140.8 Ωcm^2) than the 650 nm thick Sb_2S_3 film (77.9 Ωcm^2) indicating a higher charge recombinations in thicker Sb_2S_3 films than the thinner Sb_2S_3 films. Furthermore, as shown in surface SEM images of different Sb_2S_3 films (Figure S3), thinner Sb_2S_3 films are less compact than thicker Sb_2S_3 films, and thus thinner Sb_2S_3 films may have better penetration of hole-transport material and full coverage of HTL on Sb_2S_3 nanostructures, which may improve charge collection efficiency. As a result, while increasing Sb_2S_3 thickness may absorb more photons and thus deliver more photocurrent, the optimum Sb_2S_3 thickness for a device with an FTO/TiO_2/Sb_2S_3/P3HT structure is 270 nm because the thickness of the Sb_2S_3 layer is determined by the balance between charge collection (R_{HTM}) and charge recombination (Rrec). On the other hand, the lifetime (τ) calculated by the Bode plot for different Sb_2S_3 thicknesses indicated a shorter life-time of 4.69 μs for a 175 nm thick Sb_2S_3 film while with the increase of the Sb_2S_3 thickness to 270 nm, the life-time increases to 6.82 and further increase of the thickness to 380–650 nm, the life-time decreases. The observation supports that the charge recombination in thicker Sb_2S_3 films are higher than the thinner Sb_2S_3 films which could be due to incomplete penetration of HTM in thicker

Table 4

The electronic properties of P3HT, SpiroOMeTAD, and CuSCN (Jain et al., 2019; Deng et al., 2020; Lv et al., 2020).

HTM	Energygap (eV)	Conductivity (S cm^{-1})	Hole Mobility (cm^2 V^{-1} S^{-1})	Hole Diffusion Co-efficient (cm^2 s^{-1})	VBM$_{HTL}$ (eV)	CBM$_{HTL}$ (eV)
P3HT	1.7	1×10^{-5}	1×10^{-4}	1.8×10^{-3}	-5.2	-3.5
SpiroOMeTAD	3.1	5.92×10^{-4}	2×10^{-5}	2.3	-5.2	-2.1
CuSCN	3.5	10^{-2}	1×10^{-1}	5.2×10^{-6}	-5.3	-1.8

Table 5

SpiroOMTAD layer thickness dependent photovoltaic performance of the devices FTO/TiO$_2$/Sb$_2$S$_3$/P3HT/Ag measured under one Sun AM 1.5G illumination.

HTM layer Thickness (nm)	Voc (V)	Jsc (mA/cm^2)	FF (%)	η (%)
80	600.2	14.1	43.8	3.70
100	603.1	15.6	43.6	4.11
120	613.4	12.5	40.7	3.12

Sb$_2$S$_3$ films that would resulting in inferior charge separation in excitons.

The observed 4.01 % efficiency for the optimised ETL and Sb$_2$S$_3$ layerswith a Voc of 619.2 mV, Jsc of 14.05 mA/cm^2 and FF of 46.1 %, indicate that the observed photovoltacis performances are significantly lower than the theoretically predicted solar cell performance for a single p-n junction FTO/TiO$_2$/Sb$_2$S$_3$/P3HT solar cells. Hence, by using and optimizing the best HTL, one can improve charge transport and collection because the HTL acts as an energy barrier to prevent electron transfer to the cathode and, the efficiency of holes extraction in the active layer to the electrode is dependent on the properties of the HTL. Furthermore, a well-matched highest occupied molecular orbital (HOMO) energy level in HTL that matches the energy levels of Sb$_2$S$_3$ layer can aid in improving the open circuit voltage (Voc). Because the best PCE of the Sb$_2$S$_3$ cell was theoretically predicted with the VBM$_{HTL}$ at − 6.1 eV, the most common HTL, such as P3HT, SpiroOMTAD, and CuCNS, were chosen for HTL optimization because their electronic properties, as shown in Table 4, matched the theoretical predictions. The variation of Voc, Jsc, FF, and η with varying the thicknesses of SpiroOMTAD layer of the device FTO/TiO$_2$/Sb$_2$S$_3$/SpiroOMTAD structure and having ETL and Sb$_2$S$_3$ layers thicknesses of 105 and 270 nm respectively is given in Table 5 and the highest solar cell efficiency of 4.11 % was observed for ~100 nm thick HTL.

The observed variation of solar cell performance with the variation on SpiroOMTAD layer thickness indicate a thicker HTL resulting in the rapid decrease in Jsc and FF which could be assigned to the increase in series resistance of a thicker SpiroOMTAD layer leading to rapid charge recombination and consequently the observed lower solar cell performance can be justified. On the other hand, as shown in Fig. 6 and the device performance summarized in the Table 6 for devices which was fabricated with different HTLs indicate the photovoltaic performance of Sb$_2$S$_3$ solar cell is highly depend on the HTL type, indicating that the hole transfer across the Sb$_2$S$_3$–HTL interface, hole-conductivity, and diffusion (mobility) of holes plays a significant role in optimizing the performance of Sb$_2$S$_3$ solar cells. With SpiroOMeTAD as a hole conductor, Sb$_2$S$_3$ thin film demonstrated the best solar cell performance, while P3HT demonstrated comparable solar cell performance and CuSCN demonstrated dismissal solar cell performance. The champion cell with SpiroOMeTAD reached a 4.11 % efficiency, with a Voc of 603.1 mV, Jsc of 15.6 mA/cm^2 and FF of 43.6 %.

As shown in Fig. 6a, and Table 6, the photovoltaic performance of Sb$_2$S$_3$ solar cell is highly depend on the HTL type, indicating that the hole transfer across the Sb$_2$S$_3$–HTL interface, hole-conductivity, and diffusion (mobility) of holes plays a significant role in optimizing the performance of Sb$_2$S$_3$ solar cells. With SpiroOMeTAD as a hole conductor, Sb$_2$S$_3$ thin film demonstrated the best solar cell performance, while P3HT demonstrated comparable solar cell performance and CuSCN demonstrated dismissal solar cell performance. The champion cell with SpiroOMeTAD reached a 4.11 % efficiency, with a Voc of 603.1 mV, Jsc of 15.6 mA/cm^2 and FF of 43.6 %.

The optimized device was obtained with TiO2 (108 μm), Sb$_2$S$_3$ (270 nm) and SpiroOMeTAD (100 nm). The EQE measurements of Sb$_2$S$_3$ with different HTL shown in Fig. 6b confirm the observed JV variations shown in Fig. 6a. The observed higher Jsc with SpiroOMeTAD and P3HT than CuSCN cannot be explained solely by thermodynamic factors because the free energy difference in each case is thermodynamically equal, taking into account the VBM$_{HTL}$ positions of CuSCN (-5.3 eV), P3HT (-5.2 eV) and SpiroOMeTAD (-5.2 eV). Similarly, the observed differences in Voc of the cells could not be simply attributed to

Table 6

Various HTLs dependent photovoltaic performance of the devices FTO/TiO$_2$/Sb$_2$S$_3$/P3HT/Ag measured under one Sun AM 1.5G illumination.

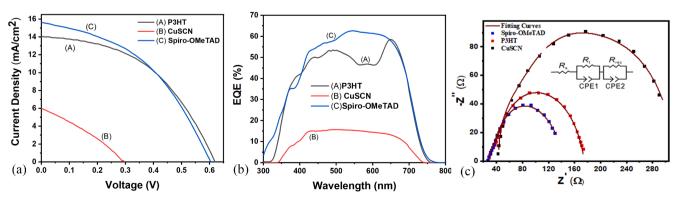| HTM	Voc (V)	Jsc (mA/cm^2)	FF (%)	η (%)
CuSCN	295.2	6.01	30.7	0.55
P3HT	619.2	14.05	46.1	4.01
Spiro	603.1	15.6	43.6	4.11

Fig. 6. (a) J-V characteristic curves, (b) IPCE spectra (b), and (c) EIS plot for the devices with different HTM.

Table 7
Fitting results of the EIS spectra of the devices with different HTLs.

HTM	Rs (Ω)	R_t (Ω)	R_{rec} (Ω)
CuSCN	43.1	26.9	216
P3HT	29.2	7.56	139
SpiroOMeTAD	27.6	5.16	110

differences in the HOMO energy level of the HTM since they are alike. According to Christian et al., the efficiency of hole collection is highly dependent on the Sb_2S_3–HTL interfacial properties, as demonstrated further by modeling results in which interfacial hole transfer, rather than diffusion in Sb_2S_3, is found to be the dominant factor dictating the magnitude of the hole transfer rate for equal thick Sb_2S_3 films. (Christians and Kamat, 2013; Christians et al., 2014).

According to the hole conductor properties shown in Table 4, CuSCNS has superior conductivity when compared to P3HT and SpiroOMeTAD, and thus the overall poor CuSCN solar cell performance could be attributed to the Sb_2S_3–HTL interfacial properties, which may hinder facile hole transfer due to the formation of large CuCNS crystals. It could have originated from CuCNS's high series resistance and short hole diffusion length, which is consistent with the findings of Boix et al., (Boix et al., 2012) who identified CuSCN as the source of high series resistance and low FF. The large crystal may reduce the interface area while still providing a high series resistance.

The absence of parasite absorption by SpiroOMeTAD, on the other hand, improves the solar cell performance of thin Sb_2S_3 films (~270 nm) with SpiroOMeTAD over P3HT. Fig. 6b shows that the higher band gap P3HT absorbs parasitically in the 500–650 nm region more than the SpiroOMeTAD. Hence, the increased EQE and thus increased Jsc for the Sb_2S_3/SpiroOMeTAD device in the 500–650 nm range could be attributed to the absence of parasite effect; however, at longer wavelengths, the enhancement is less pronounced because more light has already been absorbed by the Sb_2S_3 film. Furthermore, due to relatively low conductivity and low hole mobility, devices using P3HT as HTMs typically exhibit low conversion efficiency, resulting in significant ohmic losses across the HTM, lowering solar cell performance. Hence, the improved solar cell performance of SpiroOMeTAD with Sb_2S_3 can be attributed to an increase in SpiroOMeTAD/Sb_2S_3 conductivity due to strong interaction of SpiroOMeTAD-Sb_2S_3 via S bonds. According to Du et al., the spiroMeTAD:Sb_2S_3 HTL exhibits enhanced conductivity due to strong electric interactions between S atoms of Sb_2S_3 and CH_3 group of spiroOMeTAD resulting in enhancement in the density of states (DOS) in the spiroOMeTAD bandgap, that would significantly enhance the conductivity of spiroOMeTAD. (Du et al., 2021).

Electrochemical impedance spectrum under light condition is measured to further investigate the interface charge transfer processes of different HTLs and Sb_2S_3. The measured EIS results are shown in Fig. 6c, and the fitting parameters are listed in Table 7. The equivalent electronic circuit used to fit the impedance spectra is shown in the inset of Fig. 6c. The data show two arcs, one at high frequency representing the contribution of HTM (Rt hole transport and extraction resistance at the cathode and the other reflecting the charge transfer resistance of the charge recombination process at the photoelectrode-HTL interface (R_{rec}), the double layer capacitance at the electrode–electrolyte interface, and the Warburg function, respectively. Among the devices tested, the high Rs and charge transfer resistances are the main reason for the poor performance of the device with CuSCN. The low Rs, R_t, and R_{rec} values of P3HT and SpiroOMeTAD make them more suitable HTMs in Sb_2S_3 based solar cells than CuSCN. By comparing the devices with P3HT and SpiroOMeTAD as HTMs, a slight variations were noted in the Rs and R_{rec} values while R_t shows significant variation, which implies that a good extraction of holes at Sb_2S_3/SpiroOMeTAD phase compared to Sb_2S_3/P3HT. As shown in surface images of bare and spiro coated Sb_2S_3 films in Fig. 7a and b respectively, the bare Sb_2S_3 has characteristic coarse grain morphology while in the case of SpiroOMeTAD coated Sb_2S_3 film, the SpiroOMeTAD is completely covered with the Sb_2S_3 layer enabling effective transfer of photo-generated electron-hole pairs to the electrodes which could increase the device performance.

4. Conclusion

The ETL, light harvesting Sb_2S_3 layer as well as the HTL of the planar device structure FTO/TiO_2(ETL)/Sb_2S_3/P3HT(HTL) were systematically investigated to realize the performance predicted by the theoretical simulations of Sb_2S_3 based solar cells. The 4.11 % efficiency (with JSC = 15.6 mA/cm^2, VOC = 0.603 V, FF = 43.6 %) achieved in this investigation via the optimization of ETL (108 nm), Sb_2S_3 (270 nm) and HTL (100 nm) is much inferior to the theoretical and simulated efficiency of ~28.64 %, (with JSC = 22.46 mA/cm^2, VOC = 1.402 V, FF = 91 %) under an AM 1.5G and 1000 W/m^2 spectral irradiance. Among the simulated and experimental PEC performances, the highest discrepancies were noted with Voc (56.9 %) and FF (52.7 %) while the discrepancy was minimal (30.5 %) with the observed Jsc. Although, the thickness of light harvesting Sb_2S_3 layer is a critical factor, the absorption is not the only factor influencing Jsc as the Jsc is determined by the balance between the thickness of Sb_2S_3 and the electron/hole diffusion lengths. On the other hand, the recombination mechanisms at both Sb_2S_3 bulk and interface, a non-ideal band alignment, the formation of defects at semiconductor/metal contact could be the reason for lower Voc and FF and hence investigation should be concentrated on these factors in order to achieve the theoretically predicated PEC performance.
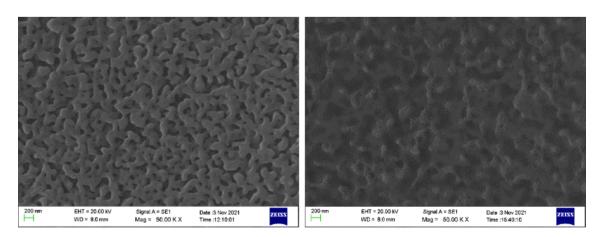

Fig. 7. Surface SEM images of (a) Sb_2S_3 film and (b) SpiroOMeTAD coated Sb_2S_3 films.

Declaration of Competing Interest

The authors declare that they have no known competing financial interests or personal relationships that could have appeared to influence the work reported in this paper.

Acknowledgement

Appendix A. Supplementary data

Supplementary data to this article can be found online at https://doi.org/10.1016/j.solener.2022.10.025.

References

Boix, P.P., Lee, Y.H., Fabregat-Santiago, F., Im, S.H., Mora-Sero, I., Bisquert, J., Seok, S.I., 2012. From flat to nanostructured photovoltaics: balance between thickness of the absorber and charge screening in sensitized solar cells. ACS Nano 6, 873–880.

Brennan, T.P., Ardalan, P., Lee, H.B.R., Bakke, J.R., Ding, I.K., McGehee, M.D., Bent, S.F., 2011. Atomic Layer Deposition of CdS Quantum Dots for Solid-State Quantum Dot Sensitized Solar Cells. Adv. Energy Mater. 1, 1169–1175.

Büttner, P., Scheler, F., Pointer, C., Döhler, D., Yokosawa, T., Spiecker, E., Boix, P.P., Young, E.R., Mínguez-Bacho, I., Bachmann, J., 2021. ZnS Ultrathin Interfacial Layers for Optimizing Carrier Management in Sb2S3-based Photovoltaics. ACS Appl. Mater. Interfaces 13, 11861–11868.

Cai, Z., Dai, C.-M., Chen, S., 2020. Intrinsic defect limit to the electrical conductivity and a two-step p-type doping strategy for overcoming the efficiency bottleneck of Sb2S3-based solar cells. Solar RRL 4, 1900503.

Cao, Y., Zhu, X., Jiang, J., Liu, C., Zhou, J., Ni, J., Zhang, J., Pang, J., 2020. Rotational design of charge carrier transport layers for optimal antimony trisulfide solar cells and its integration in tandem devices. Sol. Energy Mater. Sol. Cells 206, 110279.

Choi, Y.C., Lee, D.U., Noh, J.H., Kim, E.K., Seok, S.I., 2014. Highly improved Sb2S3 sensitized-inorganic–organic heterojunction solar cells and quantification of traps by deep-level transient spectroscopy. Adv. Funct. Mater. 24, 3587–3592.

Christians, J.A., Kamat, P.V., 2013. Trap and transfer. Two-step hole injection across the Sb2S3/CuSCN interface in solid-state solar cells. ACS Nano 7, 7967–7974.

Christians, J.A., Leighton, D.T., Kamat, P.V., 2014. Rate limiting interfacial hole transfer in Sb 2 S 3 solid-state solar cells. Energy Environ. Sci. 7, 1148–1158.

Courel, M., Jiménez, T., Arce-Plaza, A., Seuret-Jiménez, D., Morán-Lázaro, J., Sánchez-Rodríguez, F., 2019. A theoretical study on Sb2S3 solar cells: The path to overcome the efficiency barrier of 8%. Sol. Energy Mater. Sol. Cells 201, 110123.

DeAngelis, A.D., Kemp, K.C., Gaillard, N., Kim, K.S., 2016. Antimony (III) sulfide thin films as a photoanode material in photocatalytic water splitting. ACS Appl. Mater. Interfaces 8, 8445–8451.

Deng, J., Peng, C., Dai, M., Lin, D., Ali, I., Alhewairini, S.S., Zheng, X., Chen, G., Li, J., Naz, I., 2020. Recent development of super-wettable materials and their applications in oil-water separation. J. Cleaner Prod. 121624.

J. Dong, Y. Liu, Z. Wang, Y. Zhang, Boosting VOC of antimony chalcogenide solar cells: A review on interfaces and defects, Nano Select, (2021).

Du, Q., Shen, Z., Chen, C., Li, F., Jin, M., Li, H., Dong, C., Zheng, J., Ji, M., Wang, M., 2021. Spiro-OMeTAD: Sb2S3 Hole Transport Layer with Triple Functions of Overcoming Lithium Salt Aggregation. Long-Term High Conductivity, and Defect Passivation for Perovskite Solar Cells, Solar RRL 5, 2100622.

Eensalu, J.S., Katerski, A., Kärber, E., Acik, I.O., Mere, A., Krunks, M., 2019. Uniform Sb2S3 optical coatings by chemical spray method. Beilstein J. Nanotechnol. 10, 198–210.

Eensalu, J.S., Katerski, A., Kärber, E., Weinhardt, L., Blum, M., Heske, C., Yang, W., Acik, I.O., Krunks, M., 2019. Semitransparent Sb2S3 thin film solar cells by ultrasonic spray pyrolysis for use in solar windows. Beilstein J. Nanotechnol. 10, 2396–2409.

Green, M.A., Dunlop, E.D., Hohl-Ebinger, J., Yoshita, M., Kopidakis, N., Hao, X., 2020. Solar cell efficiency tables (version 56). Prog. Photovoltaics Res. Appl. 28, 629–638.

Guo, L., Zhang, B., Li, S., Zhang, Q., Buettner, M., Li, L., Qian, X., Yan, F., 2019. Scalable and efficient Sb2S3 thin-film solar cells fabricated by close space sublimation. APL Mater. 7, 041105.

Han, J., Wang, S., Yang, J., Guo, S., Cao, Q., Tang, H., Pu, X., Gao, B., Li, X., 2019. Solution-processed Sb2S3 planar thin film solar cells with a conversion efficiency of 6.9% at an open circuit voltage of 0.7 V achieved via surface passivation by a SbCl3 interface layer. ACS Appl. Mater. Interfaces 12, 4970–4979.

Horoz, S., Sahin, O., 2017. Synthesis, characterization and photovoltaic properties of Mn-doped SbS thin film. Materials Science-Poland 35, 861–867.

Islam, M., Thakur, A., 2020. Two stage modelling of solar photovoltaic cells based on Sb2S3 absorber with three distinct buffer combinations. Sol. Energy 202, 304–315.

Jain, S.M., Edvinsson, T., Durrant, J.R., 2019. Green fabrication of stable lead-free bismuth based perovskite solar cells using a non-toxic solvent, Communications. Chemistry 2, 1–7.

Kim, D.-H., Lee, S.-J., Park, M.S., Kang, J.-K., Heo, J.H., Im, S.H., Sung, S.-J., 2014. Highly reproducible planar Sb 2 S 3-sensitized solar cells based on atomic layer deposition. Nanoscale 6, 14549–14554.

M. Lakhe, G. Bhand, P. Londhe, A. Rohom, N. Chaure, Electrochemical synthesis and characterization of Cu2ZnSnS4 thin films, J Material Sci Eng, 5 (2016) 2169-0022.10002.

Li, K., Lu, Y., Ke, X., Li, S., Lu, S., Wang, C., Wang, S., Chen, C., Tang, J., 2020. Over 7% Efficiency of Sb2 (S, Se) 3 Solar Cells via V-Shaped Bandgap Engineering. Solar RRL 4, 2000220.

Lu, K., Wang, Y., Liu, Z., Han, L., Shi, G., Fang, H., Chen, J., Ye, X., Chen, S., Yang, F., 2018. High-Efficiency PbS Quantum-Dot Solar Cells with Greatly Simplified Fabrication Processing via "Solvent-Curing". Adv. Mater. 30, 1707572.

Lv, Y., Jin, Y., Cai, W., Zhang, Z., Zhou, X., Chen, H., 2020. Air-processed carbon-based perovskite solar cells with enhanced efficiency and stability: Effect of temperature control and using CuSCN. J. Alloy. Compd. 821, 153272.

Maiti, A., Chatterjee, S., Pal, A.J., 2019. Sulfur-vacancy passivation in solution-processed Sb2S3 thin films: influence on photovoltaic interfaces. ACS Applied Energy Materials 3, 810–821.

Powalla, M., Paetel, S., Hariskos, D., Wuerz, R., Kessler, F., Lechner, P., Wischmann, W., Friedlmeier, T.M., 2017. Advances in cost-efficient thin-film photovoltaics based on Cu (In, Ga) Se2. Engineering 3, 445–451.

Rühle, S., 2016. Tabulated values of the Shockley-Queisser limit for single junction solar cells. Sol. Energy 130, 139–147.

Savadogo, O., Mandal, K., 1994. Fabrication of low-cost n-Sb2S3/p-Ge heterojunction solar cells. J. Phys. D Appl. Phys. 27, 1070.

Shah, U.A., Chen, S., Khalaf, G.M.G., Jin, Z., Song, H., 2021. Wide Bandgap Sb2S3 Solar Cells. Adv. Funct. Mater. 2100265.

Shi, J., Wang, Y., Yang, M., Gu, Y., An, W., Men, Y., Yang, J., Rui, Y., 2021. Enhanced interface properties of solution-processed antimony sulfide planar solar cells with n-type indium sulfide buffer layer. Electrochim. Acta 376, 138031.

Tian, Y., Zhang, Y., Lin, Y., Gao, K., Zhang, Y., Liu, K., Yang, Q., Zhou, X., Qin, D., Wu, H., 2013. Solution-processed efficient CdTe nanocrystal/CBD-CdS hetero-junction solar cells with ZnO interlayer. J. Nanopart. Res. 15, 1–9.

Wang, Q., Chen, Z., Wang, J., Xu, Y., Wei, Y., Wei, Y., Qiu, L., Lu, H., Ding, Y., Zhu, J., 2019. Sb 2 S 3 solar cells: functional layer preparation and device performance, Inorganic Chemistry. Frontiers 6, 3381–3397.

Wu, F., Pathak, R., Jiang, L., Chen, W., Chen, C., Tong, Y., Zhang, T., Jian, R., Qiao, Q., 2019. Sb 2 S 3 Thickness-Related Photocurrent and Optoelectronic Processes in TiO 2/Sb 2 S 3/P3HT Planar Hybrid Solar Cells. Nanoscale Res. Lett. 14, 1–10.

Xiao, Y., Wang, H., Kuang, H., 2020. Numerical simulation and performance optimization of Sb2S3 solar cell with a hole transport layer. Opt. Mater. 108, 110414.

Xu, Y., Chen, W., Ding, X., Pan, X., Hu, L., Yang, S., Zhu, J., Dai, S., 2018. An ultrathin SiO 2 blocking layer to suppress interfacial recombination for efficient Sb 2 S 3-sensitized solar cells, Inorganic Chemistry. Frontiers 5, 1370–1377.

Xu, M., Wachters, A.J., van Deelen, J., Mourad, M.C., Buskens, P.J., 2014. A study on the optics of copper indium gallium (di) selenide (CIGS) solar cells with ultra-thin absorber layers. Opt. Express 22, A425–A437.

Yaghoobi Nia, N., Lamanna, E., Zendehdel, M., Palma, A.L., Zurlo, F., Castriotta, L.A., Di Carlo, A., 2019. Doping strategy for efficient and stable triple cation hybrid perovskite solar cells and module based on poly (3-hexylthiophene) hole transport layer. Small 15, 1904399.

Yuan, S., Deng, H., Yang, X., Hu, C., Khan, J., Ye, W., Tang, J., Song, H., 2017. Postsurface selenization for high performance Sb2S3 planar thin film solar cells. ACS Photonics 4, 2862–2870.

Zeng, Y., Liu, F., Green, M., Hao, X., 2018. Fabrication of Sb 2 S 3 planar thin film solar cells with closed-space sublimation method. In: In: 2018 IEEE 7th World Conference on Photovoltaic Energy Conversion (WCPEC) (A Joint Conference of 45th IEEE PVSC, 28th PVSEC & 34th EU PVSEC). IEEE, pp. 0870–0872.

Zhou, P., Bu, T., Shi, S., Li, L., Zhang, Y., Ku, Z., Peng, Y., Zhong, J., Cheng, Y.-B., Huang, F., 2018. Efficient and stable mixed perovskite solar cells using P3HT as a hole transporting layer. J. Mater. Chem. C 6, 5733–5737.

Zhou, H., Han, J., Pu, X., Li, X., 2021. Effective additive for enhancing the performance of Sb2S3 planar thin film solar cells. J. Materiomics.